Thickness and polarization dependence of the magnetooptic signal from ultrathin ferromagnetic films

E. R. Moog, C. Liu, S. D. Bader, and J. Zak*
Materials Science Division, Building 223, Argonne National Laboratory, Argonne, Illinois 60439
(Received 23 September 1988)

Longitudinal Kerr-effect measurements using both *s*- and *p*-polarized light are presented as a function of thickness for bcc Fe films grown epitaxially on Au(100) in ultrahigh vacuum (UHV). The motivation is to explore the origins of the magnetooptic response at Fe thicknesses comparable to the depth penetration of light. Special efforts were taken to optically compensate for the birefringence of the UHV window. The compensated measurements yield the magnitude of the complex rotation $\phi_m=(\phi'^2+\phi''^2)^{1/2}$, where ϕ' and ϕ'' are the real magnetooptic rotation and the ellipticity, respectively. The results show linear initial increase of ϕ_m with thickness (up to the optical penetration depth) followed by a shallow peak and leveling off to a saturation value of the thick-film Kerr rotation. A review of the relevant theory includes the Faraday and Kerr contributions to the magnetooptic response. The Faraday contribution arises from metallic reflection from the substrate and passage back through the iron overlayer. We argue that the Faraday effect dominates the response in the ultrathin limit, while the Kerr effect controls the thick-film regime.

I. INTRODUCTION

The magnetooptic Kerr effect has recently proved to be a valuable probe in the study of surface and ultrathin-film magnetism. Hysteresis curves give detailed information about the dependence of the magnetic properties on temperature, growth conditions, and film thickness.[1-3] One issue that has been left unresolved is the interpretation of Kerr-effect signals as a function of film thickness. A peak in the Kerr-intensity signal was found[2] at an intermediate thickness for ultrathin bcc Fe films grown on Au(100). This type of peaked behavior has also been reported earlier for other systems.[4,5] The motivation for the current experiments is to investigate the origin of the peak in the rotation angle as a function of thickness.

The Kerr contribution to the rotation is due to reflection from the magnetic film. The Faraday contribution is due to transmission through the magnetic overlayer, reflection from the substrate interface, and a second transmission through the magnetic overlayer. The two contributions can, in principle, be distinguished by their different incident angle and polarization dependences. The Kerr rotations ϕ'_K for *s*- and *p*-polarized light[6] are equal in magnitude but opposite in sign, for small incident angles, and can be expressed as $\phi'_{K_s}=-\phi'_{K_p}$; while the Faraday rotation ϕ'_F is independent of polarization: $\phi'_{F_s}=\phi'_{F_p}$. These results are substantiated in the theoretical review presented in Sec. II. Also, as the Fe film thickness exceeds the optical penetration depth, the Faraday contribution would be expected to vanish. Therefore, magnetooptic measurements as a function of the thickness of the Fe film should reveal the relative Faraday and Kerr contributions.

Measurements are presented of the magnetooptic signal as a function of thickness for epitaxial, lattice-matched films of Fe grown on the (100) face of a Au single crystal in ultrahigh vacuum (UHV).[1-2] Special care was taken to compensate for the birefringence of the UHV window. The results show a linear initial increase of the signal (for thicknesses less than the penetration depth) followed by a shallow peak and a leveling off to the saturation value of the thick-film Kerr effect.

In Sec. II the relevant theory is reviewed. Experimental considerations, including the film-thickness monitoring using Auger spectroscopy and the optical compensation procedures, are presented in Sec. III. Section III also includes a description of the compensation process using the Poincaré-sphere representation of the light polarization. The results and discussion appear in Sec. IV, and a brief summary appears in Sec. V.

II. THEORETICAL CONSIDERATIONS

The following review provides guidelines for understanding studies of the magnetooptic signal as a function of film thickness. The presentation is based primarily on Refs. 6–10.

A. Index of refraction in the presence of the magnetization

One can define a dielectric constant ϵ_0 in the absence of a magnetic field,

$$\mathbf{D}=\epsilon_0\mathbf{E}\ , \tag{1}$$

where $\mathbf{D}$ is the displacement and $\mathbf{E}$ the electric field vector. The quantity ϵ_0 is a scalar for an isotropic medium and is complex for an absorbing medium. In the presence of a magnetic field H, a dielectric tensor $\hat{\epsilon}$ is introduced. Its elements satisfy Onsager's relations;[7]

$$\hat{\epsilon}_{ij}(-H)=\hat{\epsilon}_{ji}(H)\ .$$

By expanding $\hat{\epsilon}$ up to linear terms in **H** one finds the following expressions:

$$\hat{\epsilon}=\hat{\epsilon}_0+\hat{\epsilon}', \quad \hat{\epsilon}'=\begin{bmatrix} 0 & \epsilon_{12} & -\epsilon_{13} \\ -\epsilon_{12} & 0 & \epsilon_{23} \\ \epsilon_{13} & -\epsilon_{23} & 0 \end{bmatrix}, \tag{2}$$

where $\hat{\epsilon}_0$ is a scalar as in Eq. (1) and $\hat{\epsilon}'$ contains three independent components (it is an antisymmetric tensor). As such, it can be expressed by an axial vector **g**. From symmetry of the isotropic medium, **g** is parallel to **H**. By using the notion of an antisymmetric unit tensor e_{ijk} we have

$$\hat{\epsilon}_{ij}=\sum_k e_{ijk}g_k \ . \tag{3}$$

The connection between the components of the dielectric tensor $\hat{\epsilon}'$ and the axial vector **g** is

$$g_3=\epsilon_{12}, \quad g_2=-\epsilon_{13}, \quad g_1=\epsilon_{23} \ .$$

When the magnetic field **H** (or **M** for a magnetized ferromagnet) is in the z direction, axial symmetry about **H** causes $\hat{\epsilon}$ to assume the form[8]

$$\hat{\epsilon}=\begin{bmatrix} \epsilon_0 & \epsilon_1 & 0 \\ -\epsilon_1 & \epsilon_0 & 0 \\ 0 & 0 & \epsilon_0 \end{bmatrix}, \quad g_3=g=\epsilon_1 \ , \tag{4}$$

where ϵ_{12} is now denoted by ϵ_1. In the coordinate system with $\mathbf{H}\|\mathbf{z}$, $g_1=g_2=0$ and $g=g_3=\epsilon_1$. If $\hat{\epsilon}$ in Eq. (4) is known, one can find it easily in any other coordinate system. What is interesting about this approach is that there is a single vector **g** which describes the anisotropy of an isotropic medium in a magnetic field.[7]

From Maxwell's equations,[7]

$$\mathbf{D}=n^2\mathbf{E}-(\mathbf{E}\cdot\mathbf{n})\mathbf{n} \ . \tag{5}$$

On the other hand **D** is related to **E** by the dielectric tensor

$$D_i=\sum_j \hat{\epsilon}_{ij}E_j \ , \tag{6}$$

where $\hat{\epsilon}$ expresses the properties of the medium in the presence of **H**. In a magnetic field the medium becomes anisotropic. In any anisotropic medium $\mathbf{D}\perp\mathbf{n}$, where **n** is the refraction-index vector. We choose a coordinate system $x'y'z'$ in the medium with $\mathbf{z}'\|\mathbf{n}$ and y' in the plane of incidence (the yz plane), as shown in Fig. 1. In this coordinate system Eq. (5) becomes

$$E_{x'}=\frac{1}{n^2}D_{x'}, \quad E_{y'}=\frac{1}{n^2}D_{y'} \ . \tag{7}$$

From Eqs. (2), (3), and (6) we have

$$\mathbf{D}=\epsilon_0\mathbf{E}+\mathbf{E}\times\mathbf{g} \ , \tag{8}$$

where $\sum_{j,k} e_{ijk}E_jg_k$ has been used to express the vector product $\mathbf{E}\times\mathbf{g}$. To first order in the magnetic field, Eq. (8) can be inverted to give

$$\mathbf{E}=\frac{1}{\epsilon_0}\mathbf{D}-\frac{1}{\epsilon_0^2}\mathbf{D}\times\mathbf{g} \ . \tag{9}$$

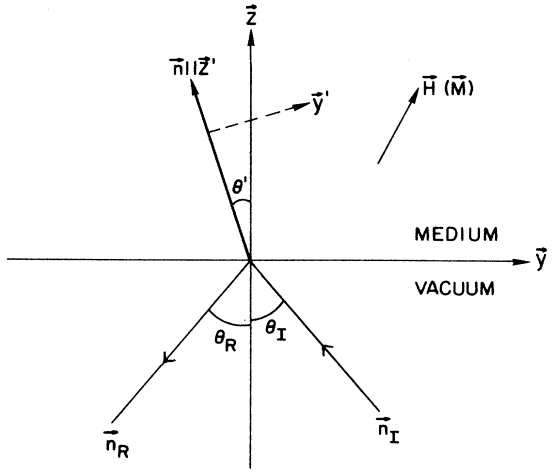

FIG. 1. Diagram of the coordinate system and geometrical terms used in the theoretical development.

While $\mathbf{D}\perp\mathbf{n}$, it follows from Eq. (9) that **E** is not perpendicular to **n** (**E** has a component in the z' direction). Comparing the components of **E** in the x' and y' directions in Eqs. (7) and (9) gives

$$\begin{aligned} &\left[\frac{1}{n^2}-\frac{1}{\epsilon_0}\right]D_{x'}+\frac{g_{z'}}{\epsilon_0^2}D_{y'}=0 \ , \\ &\frac{-g_{z'}}{\epsilon_0^2}D_{x'}+\left[\frac{1}{n^2}-\frac{1}{\epsilon_0}\right]D_{y'}=0 \ . \end{aligned} \tag{10}$$

A nonvanishing **D** gives, to terms linear in the magnetic field, two solutions for the index of refraction,

$$n_{\pm}^2=n_0^2\mp\frac{i}{n_0}(\mathbf{g}\cdot\mathbf{n}_0) \ , \tag{11}$$

where $n_0^2=\epsilon_0$ and $g_{z'}=(1/n_0)(\mathbf{g}\cdot\mathbf{n}_0)$.

B. Faraday effect

Conventionally,[9] the Faraday effect is calculated for normal incidence; here we consider the general case of oblique incidence. A linearly polarized beam incident at angle θ_I from the normal to the surface is split into two circularly polarized beams, clockwise and counterclockwise. A different index of refraction [Eq. (11)] applies to each beam, resulting in the refraction of the two beams to slightly different angles in the medium. The components n_x and n_y of these refracted beams are the same as for the incident beam. There will, however, be two different n_z which can be calculated from Eq. (11), denoted n_{+z} and n_{-z}. Correspondingly one obtains a modified Snell's law

$$\begin{aligned} (n_{+,-})_z=&(n_0^2-\sin^2\theta')^{1/2} \\ &\times\left[1\mp\frac{i}{2n_0}[g_y\sin\theta'+g_z(n_0^2-\sin^2\theta')^{1/2}]\right] . \end{aligned} \tag{12}$$

When $\mathbf{g}=\mathbf{0}$ (no magnetic field), $(n_{+,-})_z=n_{0z}$ and Eq. (12) turns into the usual Snell's law. To first order in the magnetic field, one can neglect the difference in these directions and replace both by $\mathbf{n}_0$, the direction of the refracted beam in zero magnetic field [see Eq. (11)]. The complex Faraday rotation per unit length in the $\mathbf{n}_0$ direction is[9]

$$\rho_F=\phi'_F+i\phi''_F=\frac{\omega}{2c}(n_+-n_-)\ , \tag{13}$$

where ϕ'_F is the rotation and ϕ''_F the ellipticity of the Faraday effect (for ϕ''_F small[9]).

Inserting the values of Eq. (11) for n_+ and n_- into Eq. (13), for H in the plane of incidence of the light and in the plane of the surface ($H\|y$), gives

$$\rho_F=\frac{-i\omega}{2cn_0^2}\mathbf{g}\cdot\mathbf{n}_0=\frac{i\omega}{2n_0c}g\sin\theta'$$

or in the notation of Ref. 8, the Faraday rotation ϕ'_F is

$$\phi'_F=\frac{-\omega\sin\theta'}{2c}\mathrm{Im}\left[\frac{\epsilon_1}{n_0}\right]\ . \tag{14}$$

Note that if the beam passes through the magnetic film, is reflected, and then passes through the film again, the Faraday rotation is doubled.

C. Kerr effect

The formulas for the Kerr effect were derived in much detail by Metzger *et al.*,[6] where expressions to second order in the magnetization are given. Although the results summarized here will be to first order only, we note that including the second-order effects becomes important in the case of antiferromagnetism. To begin, we consider a general direction of the magnetic field (or magnetization), given by the cosines a, b, and c of the field in the x, y, and z directions, respectively. The two polarizations of the incident light are considered separately. The expressions from Ref. 6 will be rewritten here in a more commonly used notation.[8,9] The constants $\hat{n}_0$, Q, β_0, γ_0 used in Ref. 6 are connected to the constants used here by

$$\hat{n}_0=n_0=\sqrt{\epsilon_0}\ ,$$
$$i\hat{n}_0^2Q=\epsilon_1=g\ ,$$
$$\hat{n}_0\beta_0=\sin\theta_I\ ,$$
$$\gamma_0=(1-\beta_0^2)^{1/2}\ .$$

For p polarization (the electric field of the incident light is polarized in the plane of incidence), the complex Kerr rotation ρ_p is expressed as

$$\rho_p=\frac{-g}{\epsilon_0-1}\times\frac{c(\epsilon_0-\sin^2\theta_I)^{1/2}+b\sin\theta_I}{\epsilon_0-\sin^2\theta_I-(\epsilon_0-\sin^2\theta_I)^{1/2}\sin\theta_I\tan\theta_I}\ , \tag{15}$$

where θ_I is the angle of incidence, as shown in Fig. 1. The corresponding expression for s polarization (the electric field is polarized normal to the plane of incidence), is

$$\rho_s=\frac{g}{\epsilon_0-1}\times\frac{c(\epsilon_0-\sin^2\theta_I)^{1/2}-b\sin\theta_I}{\epsilon_0-\sin^2\theta_I+(\epsilon_0-\sin^2\theta_I)^{1/2}\sin\theta_I\tan\theta_I}\ . \tag{16}$$

The Kerr rotations ϕ'_K and ellipticities ϕ''_K are expressed as

$$\rho_p=-\phi'_{K_p}+i\phi''_{K_p},\quad \rho_s=\phi'_{K_s}+i\phi''_{K_s}\ . \tag{17}$$

Thus for the Kerr rotation we have from Eqs. (17)

$$\phi'_{K_p}=-\mathrm{Re}(\rho_p),\quad \phi'_{K_s}=\mathrm{Re}(\rho_s)\ . \tag{18}$$

For an absorbing material, which must be the case for there to be a Kerr rotation, both ϵ_0 and ϵ_1 are complex. (For a nonabsorbing material, ϵ_0 is real and ϵ_1 is purely imaginary.)

Let us consider in more detail the longitudinal Kerr effect, in which $\mathbf{H}$ lies in the plane of incidence and is parallel to the y axis ($b=1$, $c=0$). For small θ_I (angle of incidence) ρ_p and ρ_s become

$$\rho_p=\rho_s=-\frac{g}{\epsilon_0-1}\frac{\theta_I}{\epsilon_0}\ . \tag{19}$$

It follows from Eqs. (18) and (19) that ϕ'_{K_p} and ϕ'_{K_s} are of opposite sign but equal magnitude,

$$\phi'_{K_p}=-\phi'_{K_s}\ . \tag{20}$$

While the Kerr rotation changes sign with change of polarization [Eq. (20)], the Faraday rotation [Eq. (14)] is polarization independent. This property can, in principle, be used to distinguish Kerr from Faraday rotations.

III. EXPERIMENTAL CONSIDERATIONS

A. Apparatus

The Kerr-effect apparatus, shown in Fig. 2, is similar to that described previously.[1-3] Polarized light from a He-Ne laser ($\lambda_0=6328$ Å) passes through a UHV window, is reflected from the sample back through the window, compensating optics, and an analyzing polarizer to a photodiode detector used to measure the intensity. An in-vacuum electromagnet is used to magnetize the sample in the plane of the film and in the scattering plane of the light. Hysteresis curves are obtained by measuring the photodiode intensity, with the analyzing polarizer set a few degrees ($\delta=2.35°$) away from extinction, as a function of the applied field. The Kerr intensity I_{Kerr} is defined as the change in the reflected light intensity transmitted through an analyzing polarizer for opposite magnetizations of the sample, normalized to the total intensity detected.

Fe is deposited from a resistively heated evaporation source that consists of tungsten wire wrapped around an alumina crucible containing the Fe. The Au(100) sample was mechanically and electropolished before being inserted into vacuum, and then Ar-ion bombarded and annealed *in situ*. Auger electron spectroscopy using a

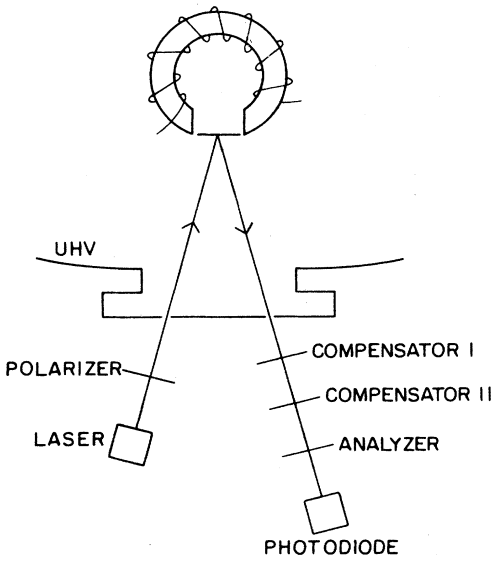

FIG. 2. Schematic drawing of the apparatus. An in-vacuum electromagnet is used to magnetize the sample. Incident laser light is *s* or *p* polarized and passes through a window into vacuum. The reflected light returns through the window, through two Soleil-Babinet compensators, and through an analyzing polarizer to a photodiode detector.

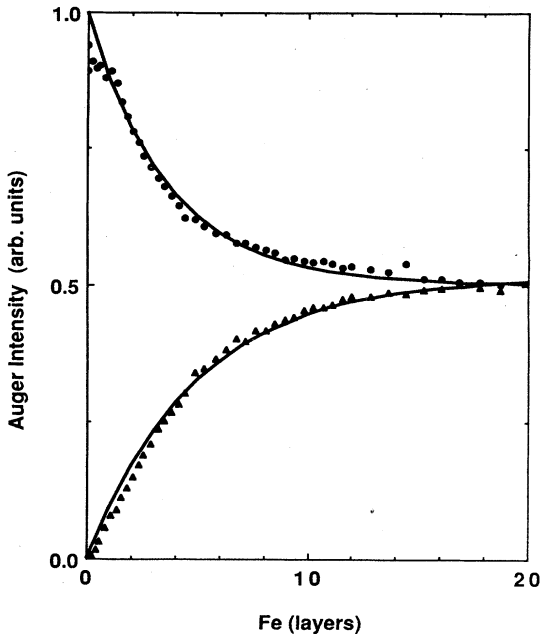

FIG. 3. Measured peak-to-peak Auger intensities for the Au 69-eV (circles) and the Fe 703-eV (triangles) transitions as the Fe deposition proceeds. The Fe intensities are doubled for clarity. The calculated curves assume ideal layer-by-layer growth with a monolayer-range film of Au segregated to the surface of the Fe.

double-pass cylindrical-mirror analyzer confirmed the cleanliness of the Au surface and was used to determine the growth rate, as described in Sec. III B.

Fe is known to grow in the bcc structure on Au(100) with the same 2.88-Å lattice spacing as bcc Fe.[1] This is because the 4.08-Å lattice constant of fcc Au yields a (100) primitive-lattice square-net spacing of $4.08/\sqrt{2} = 2.88$ Å, which coincides with that of the Fe. In these experiments the substrate temperature was held $\sim 200\,^{\circ}\mathrm{C}$ during deposition and measurement, since such elevated-temperature growth has been found to give a well-ordered surface.[1] The elevated-growth temperature promotes segregation of the Au to the iron surface, as has been shown previously.[1]

B. Film-thickness monitoring

The thickness of the Fe film is determined[11] using experimental and calculated peak-to-peak Auger intensities as a function of deposition time, as shown in Fig. 3. The evaporator provides a constant deposition rate, so that deposition time converts to thickness. The thickness scale has been fixed using a stylus profilometer (a Tencor Instruments Alpha-step 200): First, the evaporation rate was calibrated using Auger intensities, then a thick film of Fe was grown on a flat sapphire substrate, during which time periodic checks were made to confirm that the evaporation rate remained constant. The thick (830-Å) Fe film was then measured with the profilometer.

The model growth-curve calculations assume layer-by-layer growth and use the profilometer coverage calibration. The standard summation and attenuation expressions for Auger intensities are used, with an appropriate electronic mean free path λ, and with additional terms for the Au segregated to the surface. The best fits, shown in Fig. 3, use λ values of 5.16 Å for the Au 69-eV Auger electrons and 7.18 Å for the Fe 703-eV Auger electrons. The first value is in the center of the range specified by the "universal" curve used by electron spectroscopists.[12] The second value is at the low end of the "universal" curve range, but it is quite sensitive to another parameter of the fit, namely, the Auger sensitivity for pure Fe relative to that for Au. We estimate an overall uncertainty in this thickness determination of 9%.

The present monitoring procedure represents an improvement over the previously used method of empirically drawing linear segments through the measured growth curves, with the kinks that occur at the intersection of the segments being taken to represent the deposition of successive monolayers. This previous method is subject to systematic errors of interpretation if kinks occur at other than monolayer intervals, as has been reported previously[13,14] and as also occurs here in the Fe/Au system.

This same Auger fitting procedure was used previously for the system fcc Fe on Cu(100),[3] where the coverage calibration was taken from Auger kinks. We cross checked the evaporator calibration to provide additional referencing by mounting Cu(100) and Au(100) samples together in the UHV system. The coverage cross calibration agreed to within 9%. The precision within a run, of course, is much better because it involves a time measurement, and is only limited by the stability of the evaporator to deliver a constant deposition rate.

C. Optical compensation procedure

For ultrathin films the magneto-optic rotation and ellipticity are extremely small. Thus it is easier to measure the magnitude of the magneto-optic signal ϕ_m, given by

$$\phi_m = (\phi_K'^2 + \phi_K''^2)^{1/2} , \tag{21}$$

than to measure ϕ_K' and ϕ_K'' individually. For this purpose we use an optical compensation procedure based on two Soleil-Babinet compensators. The procedure also removes the UHV window birefringence. In what follows we describe the approach.

There is an unwanted birefringence affecting the polarization of the reflected light beam. It arises principally from the UHV window, which becomes birefringent when the bolts on the window flange are tightened and a vacuum is created in the chamber. There is also a contribution from the metallic reflection itself: The light incident on the sample is slightly elliptically polarized due to its passage through the window into vacuum; when light that is not purely s or p polarized reflects from a metal (even a nonmagnetic one), the reflected beam is polarized differently than the incident beam. A standard approach to correct for these unwanted alterations in the polarization of the reflected light is to use compensating optics. In the present study we used Soleil-Babinet compensators, as shown in Fig. 2. The Soleil-Babinet compensator consists of two quartz wedges pieced together to form a parallel plate. The optical axes of the wedges are orthogonal to each other and to the light path. There are two degrees of freedom that can be mechanically adjusted. First, the plate can be rotated to align the orthogonal optical axes as desired. Second, a micrometer adjustment can translate one wedge with respect to the other to provide unequal path lengths through the two wedges, and, thus, retard one orthogonal, linear polarization component with respect to the other.

Operationally, the way the compensation is achieved is to cross the analyzer and the incident laser-beam polarization. The detector does not indicate the expected extinction because the window and the magnetized sample alter the polarization. The first compensator is then introduced and its two degrees of freedom are adjusted until extinction is achieved. This means that the light that emerges from the compensator has the same (s or p) polarization as the incident light.

Ordinarily this might be the only compensation adjustment made. The polarizer could then be adjusted to its desired setting and the experiment could proceed. In the present experiments, however, a second compensator is introduced, as shown in Fig. 2. One of its optical axes is aligned parallel to the polarization direction of the laser source. This second compensator thus has no effect on the polarization associated with the original (+) magnetized state because the light exiting the first compensator is linearly polarized along one of the optical axes of the second compensator. It does, however, affect the polarization from the opposite magnetization state. A value for the second compensator retardation is chosen, the analyzer is set to the standard angle δ from extinction, and I_{Kerr} is measured. This is repeated for different retardations until a maximal I_{Kerr} is achieved, as plotted in Fig. 4. A similar compensation scheme was used in Ref. 15. Figure 5 summarizes the compensation scheme. Included in the figure is a convenient Poincaré-sphere representation of the polarization adjustments, as described below. The compensation procedure is quite laborious because the adjustments were made independently for each film thickness and laser polarization. Use of the procedure is warranted, however, because it gives quantitatively reproducible I_{Kerr} measurements, independent of the window effect, while simpler compensation methods do not.

D. Poincaré-sphere representation

The Poincaré-sphere representation[16] of polarized light provides an instructive way to understand the function of the two compensators. The Poincaré-sphere is of unit radius and its surface uniquely represents all possible states of polarization. Linear polarizations occur along the equator with longitudes corresponding to twice the angle of rotation of the light, e.g., vertical or s polarization is 180° away from horizontal or p polarization. Left and right circular polarizations occupy the north and south poles, respectively. Elliptic polarizations occur above and below the equator with the latitudes corresponding to twice the angle Ω, where $\tan\Omega = b/a$ and a and b are the major and minor axes of the ellipse. The two independent degrees of freedom of the Soleil-Babinet compensator correspond to simple geometric operations on the sphere. Setting the optical axes of the compensator corresponds to defining an axis through the origin and equator of the sphere. Adjusting the retardation of the compensator corresponds to a rotation of the sphere about the selected axis. This is shown schematically on the right-hand side of Figs. 5(b)–5(d). In Fig. 5(b), P_+ and P_- correspond to polarizations of the reflected light just before the first compensator for the two opposite sample magnetization directions. These polarizations are

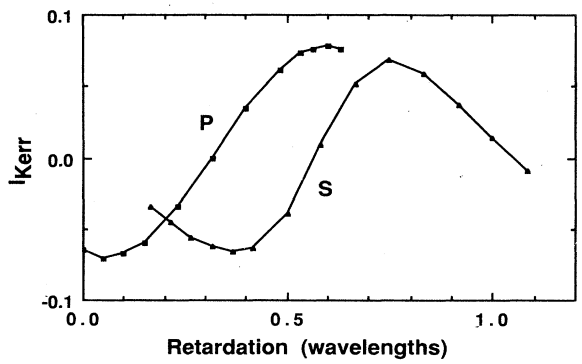

FIG. 4. Kerr intensity I_{Kerr} is plotted as a function of the retardation setting of the second compensator. The film thickness is comparable to an optical penetration depth. As the retardation varies through a full wave, I_{Kerr} oscillates sinusoidally. This shows that improper compensation of birefringence can result in a Kerr intensity of either sign and of any magnitude less than the peak value. The peak I_{Kerr} values are plotted in Fig. 6.

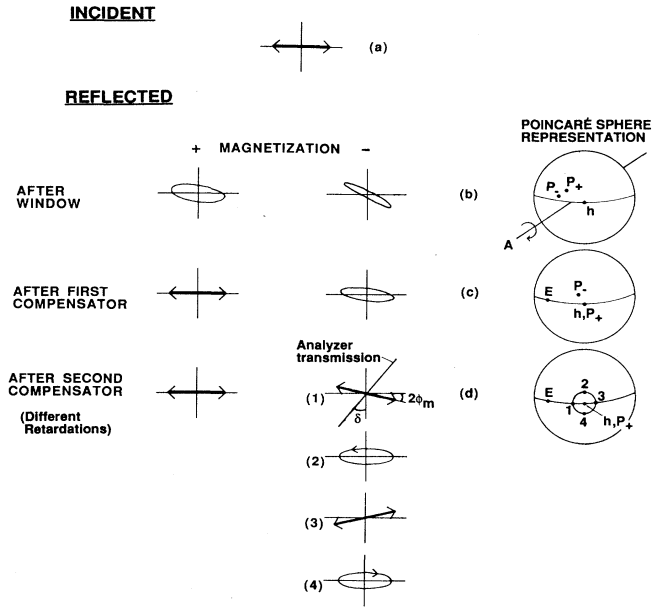

FIG. 5. Schematic of the polarization of the light at different sites along the optical path. The incident light p polarization is depicted in (a). The reflected light, shown in (b), has its polarization altered due to the UHV window birefringence and the magnetooptic interaction. The influence of the compensators is shown in (c) and (d), and, to the right, using Poincaré-sphere representations. The angle $2\phi_m$ is twice the magnitude of the complex Kerr rotation and δ is the angle between the analyzer setting and extinction E. Ellipticities and angles have been exaggerated for clarity: δ is 2.35° and ϕ is <3 min of arc.

influenced by the unknown window birefringence. The corrected values of P_+ and P_- are assumed to be linearly polarized and, in real space, separated by twice the magnitude of the magnetooptic signal $\phi_m=(\phi_K'^2+\phi_K''^2)^{1/2}$. Thus the function of the compensators is to position both P_+ and P_- on the equator of the sphere. The point h in Fig. 5(b) corresponds to horizontal or p polarization. The sphere can then be rotated about axis A so that P_+ coincides with h on the equator, as shown in Fig. 5(c). The longitudes and latitudes are exaggerated for clarity in the figure. The point E corresponds to the extinction setting of the analyzing polarizer, at angle δ from horizontal ($\delta \gg 2\phi_m$). The second compensator axis is set through the point where h and P_+ coincide, and its retardation is then adjusted to rotate the Poincaré-sphere so that the P_- traces out the circle shown in Fig. 5(d), with points 1 through 4. Since the value of I_{Kerr} is proportional to the quantity $[\sin^2(A_{P_+E}/2)-\sin^2(A_{P_-E}/2)]$, where A_{PE} is the length of the arc joining P and E on the Poincaré sphere, measuring I_{Kerr} as a function of retardation gives a sine wave with extrema of opposite sign at points 1 and 3, and zeroes at points 2 and 4. This expectation is confirmed experimentally, as shown in Fig. 4. The desired value of I_{Kerr} is that measured either at point 1 or 3, i.e., at an extremum in Fig. 4.

The Poincaré-sphere analysis of the above compensation procedure can also be carried out by a matrix technique where the action of each compensator is represented by a 2×2 matrix.[17] Details of the matrix analysis of the two compensators will be given in a separate publication. Here we summarize the results. The rotation and retardation of the first compensator are fixed by the light emerging from the UHV exit window at the + magnetization of the sample (see Fig. 5). This first compensator is set so as to make the light linearly polarized in the direction of the original laser light. The function of the second compensator is to remove a phase which depends on the window birefringence, the first compensator setting, and the ratio of ϕ_K'' and ϕ_K'.

IV. RESULTS AND DISCUSSION

A. Ultrathin Faraday regime

The magnitude of the magneto-optic signal ϕ_m is shown in Fig. 6 as a function of Fe film thickness for both s- and p-polarized light. The thickness dependence of ϕ_m can be divided into three regions: There is (i) an initial linear increase of the signal, followed by (ii) a shallow peak, and (iii) a leveling off to a saturation value of the thick-film Kerr signal. We interpret the linear region as arising from a Faraday effect for the following two reasons: First, ϕ_m is empirically found to be proportional to film thickness as in the Faraday effect. The second reason originates from the expression

$$\phi_K'+i\phi_K''=\frac{4\pi\theta_I}{\lambda_0}\frac{n_sQ}{n_s^2-1}d\ , \tag{22}$$

which is valid for small incidence angle θ_I and small thickness d ($Nd/\lambda_0 \ll 1$), where N and n_s are the indices of refraction of iron and of the substrate (Au in our case), respectively, and Q is the magnetooptic constant for Fe. Equation (22) was obtained for the small θ_I and small-d limit from the general expression for the Kerr signal in Ref. 5. It represents the linear part of the curve in Fig. 6.

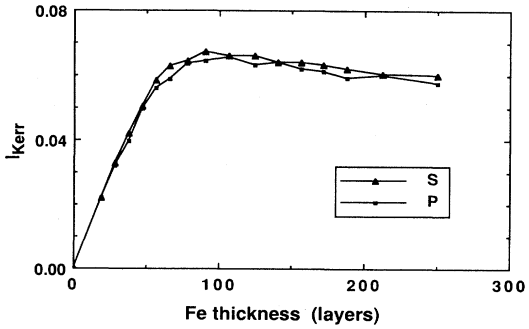

FIG. 6. Magnitude of the complex magnetooptic rotation as a function of Fe film thickness, where 1 layer = 1.44 Å. The polarizations are indicated. The initial linear increase with film thickness is due to the Faraday contribution. The saturation value in the thick limit includes only a Kerr contribution. Both Faraday and Kerr effects contribute in the intermediate region.

We now come to the second reason why this linear part should be attributed to the Faraday effect. As is well known, the Faraday rotation exists in transparent materials with a real magneto-optic constant Q, while the Kerr rotation does not[7,9] (similarly, for such materials the Faraday ellipticity is zero, while the Kerr ellipticity does not vanish). From Eq. (22) it follows that ϕ_K' is nonzero (and $\phi_K''=0$) for transparent materials with real n_s and Q. Thus, the initial linear region of Fig. 6 [see Eq. (22)] can be regarded formally as arising from a purely Faraday effect.

For a thick film Fig. 6 shows a saturation which corresponds to the "bulk" Kerr-effect value. Such a saturation appears at thicknesses exceeding the optical penetration depth ($d>90$ layers or 130 Å). For intermediate thicknesses the Faraday and Kerr effects both contribute and Fig. 6 shows a shallow peak.

The thickness dependence curve of Fig. 6 consists, therefore, of a Faraday signal (the linear part), a purely Kerr signal (the saturation part), and a combination of Faraday and Kerr signals (which lead to the intermediate part of the curve). We believe that the earlier reported peaked behavior in the magnetooptic signal as a function of the film thickness[2,4,5] is also a consequence of an interference between the Faraday and Kerr effects. The smaller peak in both sets of polarization data in Fig. 6 also originates partly from a weak reflectivity minimum, as in Refs. 5 and 18. Simulations utilizing the optical constants for Fe and Au, to be reported elsewhere,[19] support this claim.

B. Polarization effects

Figure 6 gives also the polarization dependence of the magneto-optic signal. The s and p polarizations give slightly different signals. As was pointed out in Sec. II the Faraday rotation is polarization independent, while for the Kerr rotation s and p polarizations have opposite signs for small angles [Eq. (19)]. In Fig. 6, however, the magnitude ϕ_m of the magneto-optic signal is measured [Eq. (21)] and must always be positive. The small difference between the s- and p-polarization signals observable in Fig. 6 can be attributed to optical alignment errors, and deviations from the small-angle approximation. In work to be reported elsewhere[20] we will decompose the rotation and ellipticity components of ϕ_m and discuss their polarization dependences with respect to theoretical expectations.

C. Quantification

Once the magnitude of the Kerr intensity has been determined, it can be converted into the magnitude of the complex Kerr rotation. The Kerr intensity is defined to be the intensity difference for the sample magnetized in opposite directions, normalized by the total polarized-light intensity,

$$I_{\mathrm{Kerr}}=\frac{I(\delta)-I(\delta-2\phi_m)}{I(\delta-\phi_m)} .$$

The expression is only valid for $\delta>\phi_m$. Since $I(\delta)\propto\sin^2(\delta)$, I_{Kerr} can be expressed as

$$I_{\mathrm{Kerr}}=\frac{\sin^2(\delta)-\sin^2(\delta-2\phi_m)}{\sin^2(\delta-\phi_m)}\approx\frac{4\phi_m(\delta-\phi_m)}{(\delta-\phi_m)^2} ,$$

for small ϕ_m and δ. Using the above expression to determine ϕ_m from the measured I_{Kerr} gives $\phi_m=2.2$ min of arc for thick Fe. Treves[21] measured a Kerr rotation for green (as opposed to red He-Ne) light of ~ 3.5 min at this same incident angle. The above expression also shows why an angle δ (2.35°) is set between the analyzing polarizer and extinction. The photodiode intensity difference for the two opposite magnetizations (the numerator in the expression) increases with increasing δ. For very small δ ($\delta\ll 1°$) the intensity difference is too small to measure experimentally. If δ becomes too large (greater than a few degrees), the noise in the intensity increases faster with δ than does the intensity difference and soon overwhelms it.

An additional method used in this paper for enhancing the magnetooptic signal is the two-compensator procedure which measures the magnitude ϕ_m [Eq. (21)]. The latter consists of the angle of rotation ϕ' and the ellipticity ϕ''. When one of them is small, while the other one is large, ϕ_m is still a large signal.

Finally, we would like to point out that the linear part of Fig. 6 is very sensitive to the refractive index of the substrate [Eq. (22)]. Correspondingly, the magnetooptic signal can be enhanced by choosing an appropriate metallic reflector for the substrate.[19] The Faraday signal (linear part in Fig. 6) should crucially depend on this choice. Strong enhancements in magnetooptic rotation as a function of wavelength have recently been reported for Fe-Cu bilayers and compositionally modulated multilayers.[22]

V. CONCLUSIONS

The magneto-optic response has been measured for s- and p-polarized light as a function of thickness for Fe films grown epitaxially on Au(100). The results show an initial linear increase in the signal, followed by a broad and shallow peak, and then saturation to the thick-film Kerr-effect value. This is in accord with simple expectation for the Faraday and the Kerr effects. The Faraday component arises from transmission through the Fe film, reflection at the Fe-Au interface, and a second transmission through the Fe film. The Kerr component appears when the film is sufficiently thick to reflect the incoming light.

ACKNOWLEDGMENTS

The authors wish to thank J. Pearson for technical assistance and M. Grimsditch for helpful discussions. This work was supported by the U.S. Department of Energy, Basic Energy Sciences–Materials Sciences, under Contract No. W-31-109-ENG-38. One of us (S.D.B.) would like to thank the Physics Department of the Technion–Israel Institute of Technology, Haifa, for its hospitality during part of the study, and the U.S.–Israel Binational Science Foundation for support. Another of us (J.Z.) would like to acknowledge the kind hospitality extended to him during his stay at Argonne National Laboratory.

*Permanent address: Department of Physics, Technion–Israel Institute of Technology, 32000 Haifa, Israel.

[1]E. R. Moog and S. D. Bader, Superlattices Microstruct. **1**, 543 (1985); S. D. Bader, E. R. Moog, and P. Grünberg, J. Magn. Magn. Mater. **53**, L295 (1986).

[2]S. D. Bader and E. R. Moog, in *Metallic Multilayers and Epitaxy,* edited by M. Hong, S. Wolf, and D. C. Gubser (The Metallurgical Society, Warrendale, 1988).

[3]E. R. Moog, S. D. Bader, P. A. Montano, G. Zajac, and T. H. Fleisch, Superlattices Microstruct. **3**, 435 (1987); S. D. Bader and E. R. Moog, J. Appl. Phys. **61**, 3729 (1987).

[4]A. J. Kolk and M. Orlovic, J. Appl. Phys. **34**, 1060 (1963); J. H. Judy, J. K. Alstad, G. Bate, and J. R. Wiitala, IEEE Trans. Magn. **MAG-4**, 401 (1968).

[5]T. Yoshino and S. Tanaka, Jpn. J. Appl. Phys. **5**, 989 (1966); S. Tanaka, T. Yoshino, and T. Takahashi, *ibid.* **5**, 994 (1966).

[6]G. Metzger, P. Pluvinage, and R. Torguet, Ann. Phys. (Paris) **10**, 5 (1965).

[7]L. D. Landau and E. M. Lifshitz, *Electrodynamics of Continuous Media* (Addison-Wesley, Reading, 1960), Chap. 11.

[8]E. A. Stern, J. C. McGroddy, and W. E. Harte, Phys. Rev. **135**, A1306 (1964).

[9]J. F. Dillon, Jr., in *Magnetic Properties of Materials,* edited by Jan Smit (McGraw-Hill, New York, 1971), p. 149–204.

[10]D. Y. Smith, in *Theoretical Aspects and New Developments in Magneto-Optics,* edited by J. T. Devreese (Plenum, New York, 1980), pp. 133–182.

[11]E. R. Moog and S. D. Bader (unpublished).

[12]C. J. Powell, J. Vac. Sci. Technol. A **3**, 1338 (1985); C. J. Powell, Surf. Sci. **44**, 29 (1974); M. P. Seah and W. A. Dench, Surf. Interface Anal. **1**, 2 (1979).

[13]C. Argile and G. E. Rhead, Thin Solid Films **67**, 299 (1980), and references therein; A. K. Green, S. Prigge, and E. Bauer, *ibid.* **52**, 163 (1978).

[14]U. Gradmann and G. Waller, Surf. Sci. **116**, 539 (1982).

[15]S. Tanaka, Jpn. J. Appl. Phys. **2**, 548 (1963).

[16]G. N. Ramachandran and S. Ramaseshan, in *Crystal Optics-Diffraction,* Vol. XXV/1 of *Handbuch der Physik,* edited by S. Flügge (Springer-Verlag, Berlin, 1961); G. N. Ramachandran and S. Rameseshan, J. Opt. Soc. Am. **42**, 49 (1952).

[17]R. Clark Jones, J. Opt. Soc. Am. **31**, 488 (1941).

[18]H. Feil and C. Haas, Phys. Rev. Lett. **58**, 65 (1987).

[19]S. D. Bader, J. Zak, and E. R. Moog (unpublished).

[20]E. R. Moog, J. Zak, M. L. Huberman, and S. D. Bader, Phys. Rev. B (to be published).

[21]D. Treves, J. Appl. Phys. **32**, 358 (1961).

[22]T. Katayama, Y. Suzuki, H. Awano, Y. Nishihara, and N. Koshizuka, Phys. Rev. Lett. **60**, 1426 (1988); K. Sato, H. Kida, and T. Katayama, Jpn. J. Appl. Phys. **27**, L237 (1988).